Smart Structures and Systems, *Vol. 28, No. 6 (2021) 839-853*
https://doi.org/10.12989/sss.2021.28.6.839

Flexible multimode pressure sensor based on liquid metal

Xiaoping Zhou* and Zihao Yu

School of Civil Engineering, Chongqing University, Chongqing 400045, China

(*Received July 6, 2021, Revised September 29, 2021, Accepted October 15, 2021*)

Abstract. In this paper, a novel multimode liquid metal-based pressure sensor is developed. The main body of the sensor is composed of polydimethylsiloxane (PDMS) elastomer. The structure of the sensor looks like a sandwich, in which the upper structure contains a cylindrical cavity, and the bottom structure contains a spiral microchannel, and the middle partition layer separates the upper and the bottom structures. Then, the liquid metal is injected into the top cavity and the bottom microchannel. Based on linear elastic fracture mechanics, the deformation of the microchannel cross-section is theoretically analyzed. The changes of resistance, capacitance, and inductance of the microchannel under pressure are deduced, and the corresponding theoretical models are established. The theoretical values of the pressure sensor are in good agreement with experimental data, implying that the developed theoretical model can explain the performance of the sensor well.

Keywords: linear regression analysis; liquid metal; multimode; pressure sensor

1. Introduction

Monitoring, evaluating and predicting the stability of geotechnical engineering have become an urgent requirement of geotechnical engineering (Wu *et al*. 2012). The safety and stability of geotechnical engineering are usually evaluated by the stress and strain states of geomaterials (Zhou *et al*. 2020). Pressure sensor is a common technology to directly obtain the internal stress distribution in key parts of rocks and soils (Springman *et al*. 2002, Palmer *et al*. 2009, Zhi *et al*. 2006, Xu *et al*. 2015). Pressure sensors used in civil engineering can be divided into the following categories according to their working principles and performance characteristics: resistive pressure sensors (Hu *et al*. 2007, Shi and Cheng 2013, Jung and Yang 2015, Gao *et al*. 2017, Zhou *et al*. 2018), capacitive pressure sensors (Wong *et al*. 2012, Won *et al*. 2015, Ali *et al*. 2016, Li *et al*. 2019), and inductive pressure sensors (Wang *et al*. 2017, Kawasetsu *et al*. 2017, 2018). However, traditional pressure sensors generally contain rigid materials and fragile electrical components, which have low mechanical durability and flexibility under cyclic loads. Therefore, it is of great significance to develop a new type of flexible pressure sensor.

In recent years, liquid metal and PDMS materials have been widely used in the field of flexible sensors. Liquid metal stress-strain sensors based on resistance principle have been widely studied (Shou *et al*. 2021, Ryu *et al*. 2011). In 2007, Hu *et al*. (2007) successfully used liquid metal as interconnect to develop a super flexible sensing skin that can sense force, and its change of resistance with pressure is about 0.3% / KG. Shi and Cheng (2013) developed an artificial hair cell sensor, in which the liquid metal piezoresistive element deforms with the elastomer substrate, and the normal force and shear force can be detected by the resistance change of the piezoresistive element. The sensor (Jung and Yang 2015) is mainly composed of liquid metal and PDMS elastomer, which has been successfully integrated into the microfluidic system with high linearity, repeatability and long-term stability. A kind of polydimethylsiloxane (PDMS) wristband with embedded microfluidic diaphragm pressure sensor (Gao *et al*. 2017) can monitor the pulse in real time, can solve the pressure change below 50 Pa with 90 ms response time under the detection limit of less than 100 Pa, and can realize the temperature self-compensation through the Wheatstone bridge, which allows the temperature change within 20-50°C. Zhou *et al*. (2018) injected conductive liquid metal eGaIn into the silicon rubber microchannel and successfully developed a super-elastic pressure sensor based on the principle of resistance. The experimental results showed that the calibration curve and equation have good linearity and low hysteresis.

Flexible capacitive pressure sensors have attracted much attention due to their high sensitivity, low power consumption and compact structure (Chuang *et al*. 2012). Wong *et al*. (2012) developed a flexible multilayer capacitive microfluidic normal force sensor by adopting a 5×5 array structure, which achieves a spatial resolution of 0.5 mm as well as stable and reliable performance. The sensor (Won *et al*. 2015) used the capacitance change caused by the overlap area between the liquid metal droplet and the flat-bottomed electrode to improve its dynamic range and sensitivity to capacitance, and successfully fabricated 36 sensing elements with a spatial resolution of 2 mm. In 2019, Li *et al*. (2019) successfully fabricated a retractable capacitive strain sensor based on thermoplastic elastomer (TPE) micro-channels. There exists a linear

*Corresponding author, Professor,
E-mail: xiao_ping_zhou@126.com

ISSN: 1738-1584 (Print), 1738-1991 (Online)

relationship between the capacitance change and the strain, and the hysteresis is small in this sensor. The use of soft polymers and liquid metals to realize flexible stress-strain sensors is a very effective method, which is now attracting more and more attention.

Soft sensing pressure sensor is another effective way. This pressure sensor includes an inductor and a sensing target. The change in the distance between the inductor and the sensing target can cause the inductance to change. At present, some scholars have developed several soft induction pressure sensors. Wang *et al*. (2017) proposed a soft induction pressure sensor based on eddy current effect composed of flexible coil and conductive film. Compared with the traditional sensor, the sensor has better soft elasticity, and the force measurement resolution reaches 0.3 mN. In 2017, Kawasetsu *et al*. (2017) simply laminated magnetorheological elastomer and non-magnetic elastomer layers on a sensor to develop a new type of flexible pressure sensor. This sensor only contains an elastomer layer and a printed circuit, so high shock resistance is achieved. A flexible three-axis pressure sensor (Kawasetsu *et al*. 2018) contains four spiral inductors and a ferromagnetic marker embedded in a cylindrical elastomer made of silicone rubber. This sensor has simple structure and good durability, which provides more possibilities for the wide application of soft induction pressure sensors.

In the prior art, resistive pressure sensors, capacitive pressure sensors, and inductive pressure sensors are all used individually, while a single-mode pressure sensor has limitations in terms of linearity and sensitivity. To solve this problem, multi-modal composite sensors have been extensively studied. Zhou *et al*. (2020) developed a multi-mode sensor that can sense strain by detecting resistance and capacitance, and compared the repeatability and linearity of the two modes. The results showed that when the sensor with the first connection method is stretched to 30% along the y-axis, both resistance and capacitance have better repeatability and linearity, but the fitting effect of resistance is better than that of capacitance. When stretched to 30% along the x-axis, the linearity of the capacitor is significantly better than that of the resistance. This means that the performance of the sensor can be fully utilized by switching between the two modes. Huang *et al*. (2016) developed a fully flexible pressure sensor based on a combined resistance and capacitance. The capacitive sensors have high sensitivity and a resolution of 0.1N, but they cannot measure large pressures. The resistive sensors can measure large pressures with a resolution of 1N, but they do not perform well in small-range pressure measurement. The sensor selectively collects resistance while acquiring capacitance. If the capacitance indicates that the pressure is less than 10 N, the resistance of the sensor is not measured. On the contrary, if the capacitance indicates that the pressure is greater than 10 N, the pressure should be determined based on the resistance. Through this method, the proposed sensor can not only measure large pressures, but also has higher resolution in a small range. The disadvantage is that both resistance and capacitance change nonlinearly with the increase of pressure. Multimode composite pressure sensors have great potential in the development of high-performance pressure sensors.

However, these sensors mentioned above still embed fragile electronic components and rigid materials in the elastomer, so stress concentration surfaces and weak interfaces inevitably occur. Under the action of long-term cyclic loads, the working performance of these sensors may obviously decrease. In addition, the previous multi-mode composite pressure sensors sense pressure by detecting resistance and capacitance, and there is no study on inductance. This paper aims to develop a new type of multi-mode flexible pressure sensor. This novel multimode liquid metal-based pressure sensor is mainly composed of PDMS elastomer, a cylindrical cavity filled with liquid metal (Galinstan, 66% Ga, 20.5% In and 13.5% Sn by weight) in the top layer, and a spiral microchannel filled with liquid metal in the bottom layer. Through two different wiring methods, the resistance, capacitance and inductance of the sensor can be measured under pressure. The hysteresis, repeatability, sensitivity cycle stability and linearity of these three pressure measurement indicators are investigated, so that appropriate pressure measurement indicators can be selected according to different application conditions. The results showed that the resistance, capacitance and inductance of the sensor developed in this paper all change linearly with the increase of pressure. The linearity of the three modes is less than 10%, and the linearity of the inductance reaches 4.32%. Compared with existing multimode pressure sensor (Huang *et al*. 2016), it has obvious advantages in linearity. In addition, the fitting effect of the capacitance of the developed sensor is better than the above-mentioned existing multimode pressure sensor. Compared with traditional flexible eddy current sensors in terms of inductive sensing, our completely soft sensor does not contain a rigid metal coil, so they have better mechanical durability and do not reduce performance due to softness under long-term cyclic loads. Moreover, in this paper, the changes of resistance, capacitance and inductance of the microchannel under pressure are studied, and corresponding theoretical models have been developed. The theoretical values of the pressure sensor are in good agreement with experimental data, indicating that the established theoretical model can explain the performance of the sensor well.

2. The basic principle

In this paper, the finite element software COMSOL multiphysics is used to numerically simulate the deformation of this developed sensor, and the compression deformation of the spiral microchannel section is shown in Fig. 1(a). The theoretical analysis of the liquid metal pressure sensor is to mainly study the relationship between the applied pressure and the change of resistance, capacitance and inductance, so as to reveal the measurement mechanism of the sensor. The mechanism of pressure sensor based on liquid metal is very complicated, so we make the following assumptions:

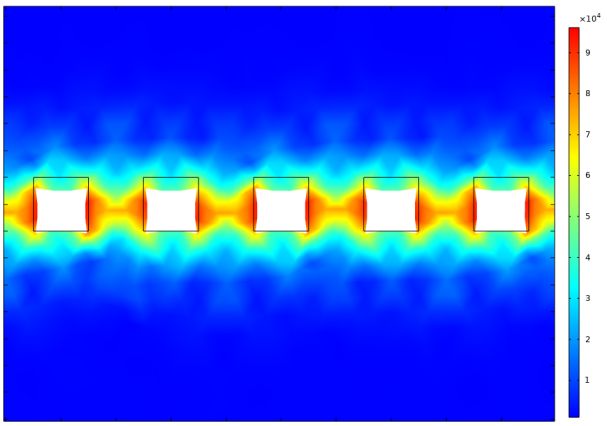

(a) Compression deformation of cross section simulated by COMSOL multiphysics

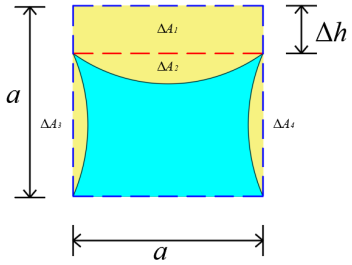

(b) The diagram of compression deformation

Fig. 1 Schematic diagrams of deformation of spiral microchannel under compression

(1) PDMS is considered as an ideal elastic material, and there is no or little residual deformation during the process of applying pressure.
(2) It is assumed that the liquid metal filled in the microchannel is incompressible.
(3) When the microchannel is filled with liquid metal, the wall of the microchannel is actually subjected to hydrostatic pressure, but it is very small and negligible compared to the pressure transmitted to the chip.
(4) Since the deformation of the upper surface of the microchannel under pressure is significantly greater than that of the lower surface, and the degree of deformation of the lower surface is relatively small, we assume that the lower surface of the microchannel does not bend under pressure.
(5) As shown in Fig. 1(b), under the condition of small deformation, it can be assumed that the deformation of the cross-sectional area of the microchannel includes four parts. The first part of the deformation is the vertical displacement Δh of the microchannel under pressure, the second part of the deformation is caused by the bending of the upper surface of the microchannel under pressure, the third and fourth parts of the deformation are caused by the bending of the sidewall of the microchannel.

2.1 The principle of resistance change

The cross-sectional area of the spiral microchannel of the sensor changes under the action of pressure, which causes a change in the resistance of the sensor. The key to studying the relationship between resistance and applied pressure is the amount of change in the cross-sectional area of the microchannel.

According to previous studies (Park *et al*. 2010), since the bottom spiral microchannel has a very small cross-sectional size, it can be regarded as a microcrack compared with the entire chip. Based on the crack stress analysis theory (Tada *et al*. 2000) and the theoretical model of contact mechanics (Shull 2002), the microchannel can be approximated as a microcrack model.

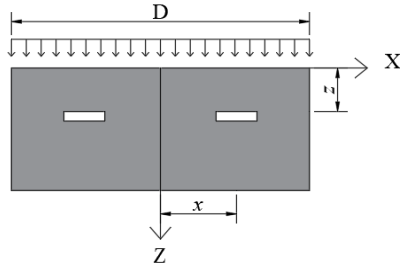

Fig. 2 The surface of the elastomer is subject to a pressure p uniformly distributed over a width D

2.1.1 The deformation of the first part

When the crack is subjected to uniform normal stress, the height between the crack faces may change. According to the Linear Elastic Fracture Mechanics (LEFM), the following equation is obtained (Park *et al*. 2010)

$$\Delta h = 2(1-\upsilon^2)a\sigma_z/E \tag{1}$$

where υ is Poisson's ratio, a is the initial cross-sectional width of the bottom spiral microchannel, and E is the Young's modulus, and σ_z is the applied stress along the Z direction.

For channels below the area of contact ($|x| < D/2$ and $z < D$), the average stress in the neighborhood of the channel may be approximated as $\sigma_z = -p$. In general, it is necessary to replace p with χp, where $\chi = \chi(x, z)$ is a correction which depends on the relative position (x, z) of the channel centerline (Park *et al*. 2010).

Then, the change in the cross-sectional area of the first part of the spiral microchannel can be estimated as

$$\Delta A_1 = 2a^2(1-\upsilon^2)\chi p/E \tag{2}$$

2.1.2 The deformation of the second part

In the case of small deformation, it is believed that the deformation of the second part is caused by the downward

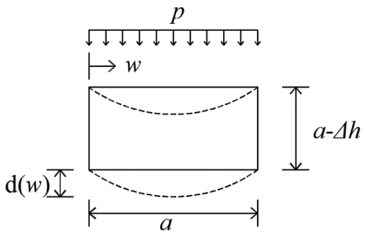

Fig. 3 Principle diagram of the deformation of the second part

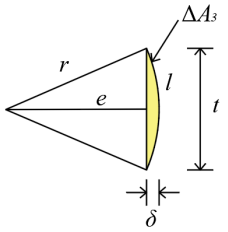

Fig. 4 Principle diagram of the deformation of the third part

bending of the flexible plate with thickness of $(a-\Delta h)$ and the length of a, as shown in Fig. 3.

The deformation of the second part is deduced by using Euler-Bernoulli beam theory, which can be written as

$$g(w)=\frac{\chi p w}{24EI}(a^3-2aw^2+w^3) \tag{3}$$

where w is the distance from the channel sidewall (Fig. 3), and EI is the bending stiffness of the flexible plate.

Therefore, the change in the cross-sectional area of the second part of the spiral microchannel can be calculated as

$$\begin{aligned}\Delta A_2 &= \int_0^a g(w)\,dw \\ &= \int_0^a \frac{\chi p w}{24EI}(a^3-2aw^2+w^3)\,dw = \frac{\chi p a^5}{120EI}\end{aligned} \tag{4}$$

2.1.3 The deformation of the third and fourth parts

We assume that the sidewall of the spiral microchannel is a smooth arc under pressure, as shown in Fig. 4.

According to the generalized Hooke's law, the stress and strain have the following relation (Rudgers 1988)

$$\begin{cases}\varepsilon_x=\frac{1}{E}\left[\sigma_x-\upsilon(\sigma_y+\sigma_z)\right]\\ \varepsilon_y=\frac{1}{E}\left[\sigma_y-\upsilon(\sigma_x+\sigma_z)\right]\\ \varepsilon_z=\frac{1}{E}\left[\sigma_z-\upsilon(\sigma_y+\sigma_x)\right]\end{cases} \tag{5}$$

where $\sigma_x,\sigma_y,\sigma_z$ are respectively the stress along x, y and z direction, and ε_x, ε_y and ε_z are respectively the strain along x, y and z direction, υ is Poisson's ratio of PDMS.

By considering the unidirectional stress state ($\sigma_x=0$, $\sigma_z=0$), it is easy to determine the following relation

$$\varepsilon_x=\varepsilon_y=-\upsilon\frac{\sigma_z}{E}=\upsilon\frac{\chi p}{E} \tag{6}$$

From Eq. (6), we have

$$\delta=a\varepsilon_y/2=\frac{\upsilon\chi p a}{2E} \tag{7}$$

According to the geometric relationship in Fig. 4, the cross-sectional area changes of the third and fourth parts of the spiral microchannel can be calculated as

$$\Delta A_3=\Delta A_4=r^2\,arcsin\left(\frac{t}{2r}\right)-\frac{te}{2} \tag{8}$$

$$e=\frac{t^2}{8\delta}-\frac{\delta}{2} \tag{9}$$

$$r=\frac{t^2}{8\delta}+\frac{\delta}{2} \tag{10}$$

$$t=a-\Delta h=a\left[1-\frac{2\chi p(1-\upsilon^2)}{E}\right] \tag{11}$$

where e, r, t and δ are the geometric parameters of the deformation area of the third part as shown in Fig. 4, E is the elastic modulus of PDMS.

Then, the total change of the cross-sectional area of the spiral microchannel can be written as

$$\Delta A=\Delta A_1+\Delta A_2+\Delta A_3+\Delta A_4 \tag{12}$$

Finally, according to Ohm's law $R=\rho L/A$, the resistance change can be estimated as

$$\Delta R=\rho L\left(\frac{1}{a^2-\Delta A}-\frac{1}{a^2}\right) \tag{13}$$

where R is the resistance of the spiral microchannel filled with liquid metal, A is the cross-sectional area of the microchannel, L is the total length of the spiral microchannel, ρ is the resistivity of the Galinstan.

2.2 The principle of capacitance change

The upper liquid metal cylinder and the liquid metal spiral microchannel at the bottom of the flexible pressure sensor developed in this paper can be regarded as a parallel plate capacitor, so the capacitance can be calculated by (Yang *et al*. 2018, Gao and Gui 2014)

$$C=\frac{\varepsilon_0\varepsilon_r S}{d} \tag{14}$$

where $\varepsilon_0=8.85\times10^{-12}$ F/m is the vacuum dielectric constant, ε_r is the relative dielectric constant of the medium in the capacitor, S is the surface area of the

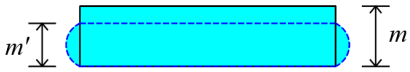

Fig. 5 Diagram of deformation of intermediate interlayer

electrodes, and d is the vertical distance between the two electrodes.

When the sensor is subjected to pressure, it is stretched in different directions. The deformation causes the surface area of the electrodes to increase and the distance between them to decrease. As a result, the capacitance of the sensor gradually increases as the pressure increases (Zhang *et al.* 2019).

The middle interlayer between the upper and lower electrodes may deform under pressure, as shown in Fig. 5.

From the aforementioned Eq. (5), the thickness of the intermediate spacer layer after deformation can be calculated as

$$m' = m(1+\varepsilon_z) = m\left(1-\frac{p}{E}\right) \tag{15}$$

where m is the initial height of the interlayer, m' is the height of the interlayer under pressure.

From the aforementioned Eq. (6), the width a' of the microchannel after deformation can be written as

$$a' = a\left(1+\varepsilon_y\right) = a\left(1+\frac{vp}{E}\right) \tag{16}$$

Then, from Eq. (14), the change of capacitance can be calculated by

$$\Delta C = C' - C_0 = \frac{\varepsilon_0\varepsilon_r Lap(1+v)}{m(E-p)} \tag{17}$$

where C is the capacitance of the sensor, L is the length of the spiral microchannel, m is the initial thickness of the sensor interlayer, a is the initial width of the microchannel, and v is the Poisson's ratio of PDMS, ε_r is the relative permittivity of PDMS.

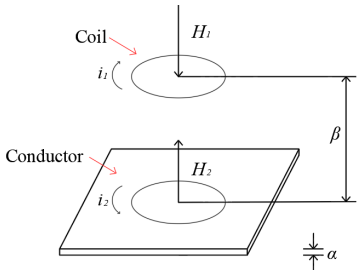

Fig. 6 The principle of eddy current sensor

2.3 The principle of inductance change

According to Faraday's law of electromagnetic induction, when an inductive coil is excited by alternating current (AC), an AC magnetic field is generated in the coil. Under the action of the AC magnetic field, a constantly changing magnetic field H_1 is generated around the coil. According to the law of electromagnetic induction, when the nearby metal conductor is close to the coil, the surface of the metal to be measured produces induced current due to the effect of the coil magnetic field, namely eddy current, as shown in Fig. 6. Under the effect of eddy current, the surface of the metal to be measured produces alternating magnetic field H_2 with opposite direction. The interaction between magnetic field H_1 and magnetic field H_2 eventually leads to the equivalent impedance, inductance, quality factor and other parameters change.

As shown in Figs. 7(a) and (b), the eddy current sensor developed in this paper is mainly composed of a bottom coil and a top metal conductor, which are used as the sensor's conversion element and sensitive element, respectively. The coil is composed of spiral microchannels filled with liquid metal, and the metal conductor is composed of a liquid metal cylinder wrapped by PDMS elastomer. Due to the strong soft elasticity of PDMS, the sensitive element may be deformed under pressure, and the size of the spiral coil can also be changed, which leads to the difference of sensor's inductance.

The electrical principle is shown in Fig. 7(d). The left loop in Fig. 7 is the sensor coil, and the right loop is the

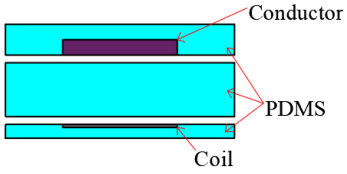

(a) Exploded view of the developed sensor

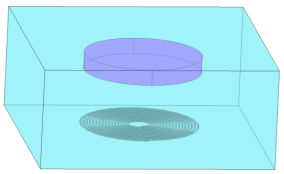

(b) 3D model of the sensor

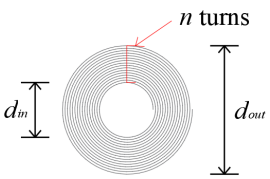

(c) Parameters of spiral coil

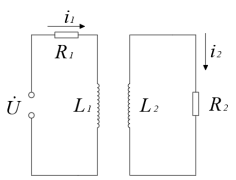

(d) Electrical schematic diagram of the developed sensor

Fig. 7 Schematic diagrams of the developed sensor

equivalent circuit of the eddy current in the measured conductor.

From Fig. 7(d), the following equation can be obtained

$$\begin{bmatrix} R_1 + j\omega L_1 & -j\omega M \\ -j\omega M & R_2 + j\omega L_2 \end{bmatrix} \begin{bmatrix} i_1 \\ i_2 \end{bmatrix} = \begin{bmatrix} \dot{U} \\ 0 \end{bmatrix} \tag{18}$$

where i_1 and i_2 are the equivalent currents in the coil and the measured conductor respectively, $\dot{U}$ is the equivalent voltage in the coil, L_1 is the inductance of the sensor coil, R_1 is the resistance of the sensor coil, L_2 is the inductance caused by the eddy current, R_2 is the resistance caused by the eddy current, $\omega = 2\pi f$ is the angular frequency of the coil excitation current, and M is the mutual inductance between the coil and the target.

From Eq. (18), the equivalent impedance and equivalent inductance of the sensor can be obtained as

$$\begin{aligned} \dot{Z} = &\left[R_1 + \frac{\omega^2 M^2}{R_2^2 + (\omega L_2)^2} R_2\right] \\ &+ j\left[\omega L_1 - \frac{\omega^2 M^2}{R_2^2 + (\omega L_2)^2} \omega L_2\right] \end{aligned} \tag{19}$$

$$L_e = L_1 - \frac{\omega^2 M^2}{R_2^2 + (\omega L_2)^2} L_2 \tag{20}$$

where $\dot{Z}$ is the equivalent impedance of the sensor, L_e is the equivalent inductance of the sensor, mutual inductance M between the coil and the target can be written as (Wang *et al*. 2014)

$$M = k(\beta)\sqrt{L_1 L_2} (0 < k < 1) \tag{21}$$

where k is the coupling factor between the primary coil and the secondary coil, which is a function of the distance β between coil and conductor (Fig. 6); the expression of $k(\beta)$ is difficult to obtain and is complex, depending on the coil geometry and target properties.

When the frequency f, or the target conductivity is larger enough, such that $\omega L_2 \gg R_2$. Then, the equivalent inductance can be expressed as (Wang *et al*. 2014)

$$L_e = [1 - k^2(\beta)] L_1 \tag{22}$$

Obviously, the inductance depends on the target position β and the coil inductance L_1. By using the surface current approximation method, the plane spiral inductance value L_1 can be calculated as (Qiao 2021).

$$L_1 = \left(\mu_0 n d_{avg} c_1/2\right)[ln(c_2/\xi) + c_3\xi + c_4\xi^2] \tag{23}$$

$$d_{avg} = (d_{out} - d_{in})/2 \tag{24}$$

$$\xi = (d_{out} - d_{in})/(d_{out} + d_{in}) \tag{25}$$

where μ_0 is the vacuum permeability coefficient, n is the number of turns of the coil, d_{avg} is the average diameter of the coil (Fig. 7(c)), d_{out} is the outer diameter of the coil, d_{in} is the inner diameter of the coil, ξ is the filling ratio of the coil.

The value of parameter c can be written as (Qiao 2021)

$$\begin{cases} c_1 = 1.00 \\ c_2 = 2.46 \\ c_3 = 0.00 \\ c_4 = 0.20 \end{cases} \tag{26}$$

Combining Eqs. (22), (23) and (26), the following equations can be obtained

$$L_1 = \left(\mu_0 n d_{avg}/2\right)[ln(2.46/\xi) + 0.2\xi^2] \tag{27}$$

$$L_e = [1 - k^2(\beta)]\{\left(\mu_0 n d_{avg}/2\right)[ln(2.46/\xi) + 0.2\xi^2]\} \tag{28}$$

The coil is composed of spiral microchannels filled with liquid metal, so the size of the coil will change under pressure. According to Eq. (5), the average diameter d'_{avg} and filling ratio ξ' of the deformed coil are

$$d'_{avg} = \left(1 + \frac{vp}{E}\right)(d_{out} - d_{in})/2 \tag{29}$$

$$\xi' = \xi = (d_{out} - d_{in})/(d_{out} + d_{in}) \tag{30}$$

where v is the Poisson's ratio of PDMS, d'_{avg} and ξ' are the average diameter and filling ratio of the deformed coil, respectively.

In the same way, the distance β' between the coil and the conductor after deformation is

$$\beta' = \beta\left(1 - \frac{p}{E}\right) \tag{31}$$

Then, the change in the equivalent inductance of the sensor under pressure can be calculated as

$$\Delta L_e = L_e{}' - L_{e_0} = L_e\left(\beta', d'_{avg}\right) - L_e\left(\beta, d_{avg}\right) \tag{32}$$

where $L_e{}'$ is the equivalent inductance after deformation, L_{e_0} is the equivalent inductance before deformation, β' is the distance between the coil and the conductor after deformation, and d'_{avg} is the average diameter of the coil after deformation.

Table 1 Principles of three pressure detection modes

Mode	Basic principle	Characteristic
Resistance	Ohm's Law	Simple structure; wide response range; large hysteresis and low resolution
Capacitance	Plate capacitor theory	Strong repeatability; low energy consumption; low sensitivity and slow response speed
Inductance	Eddying effect	Good linearity; high sensitivity; poor temperature stability

The basic principles and characteristics of these three pressure detection modes are summarized in Table 1. These three detection modes have their own advantages and disadvantages. The sensor developed in this article can solve the limitations of a single measurement mode by measuring resistance, capacitance and inductance under different application conditions.

3. Fabrication

The sensor developed in this paper consists of a soft elastomer (PDMS), a liquid metal cylinder embedded in the soft elastomer (PDMS) and a spiral microchannel filled with liquid metal. The sensor contains the upper, middle and lower parts, in which cylindrical cavity and spiral microchannel filled with liquid metal are wrapped in the top and bottom elastic bodies, respectively. Liquid metal is injected into the reserved cavity from the top liquid injection port to form a liquid metal cylinder with a diameter of 15 mm and a thickness of 2 mm. The liquid metal is injected into the spiral microchannel of the PDMS elastomer from the bottom liquid injection port to form an inductor. The spiral microchannel has 16 turns with an outer diameter of 15 mm and a trace spacing of 0.2 mm.

In this paper, the manufacturing process of flexible multi-mode pressure sensor contains three steps: manufacturing of master mold, polymer manufacturing and pouring, liquid metal injection and packaging. The manufacturing methods of microfluidic chips are described as follows: molding method, hot pressing method and laser etching method. Soft lithography technology (Zeng 2018) can achieve higher accuracy and lower cost, so this technology is applied to process three PMMA molds shown in Fig. 8(a). The first mold is used to cast the top layer with a cylindrical cavity, the second mold is used to cast the bottom layer with spiral microchannels, and the last mold is used to cast the intermediate layer.

A layer of release film (Zhou *et al*. 2020) (Ease Release 200, Mann Technologies) is coated on the finished mold. The developed sensor uses the method of pouring liquid PDMS on the prepared PMMA mold to prepare the microfluidic chip, which is made of prepolymer and curing agent with the ratio of 10:1 (RTV615, Momentive, Columbus, OH) (Zhou *et al*. 2018). The ratio can make it have the advantages of high elasticity and easy casting at a given curing temperature (Zhou *et al*. 2020). The PDMS curing agent and prepolymer are poured into the container and they are evenly mixed, then the liquid PDMS is placed in a vacuum desiccator for 30 minutes to remove air bubbles. Subsequently, the bubble-removed mixture is spin-coated onto the prepared PMMA mold at a speed of 500 rpm, as shown in Fig. 8(b), and the liquid PDMS is heated and cured at 75°C for 50 minutes.

These three cured PDMS layers are separated from the mold, aligned and treated with 90W oxygen plasma for 90

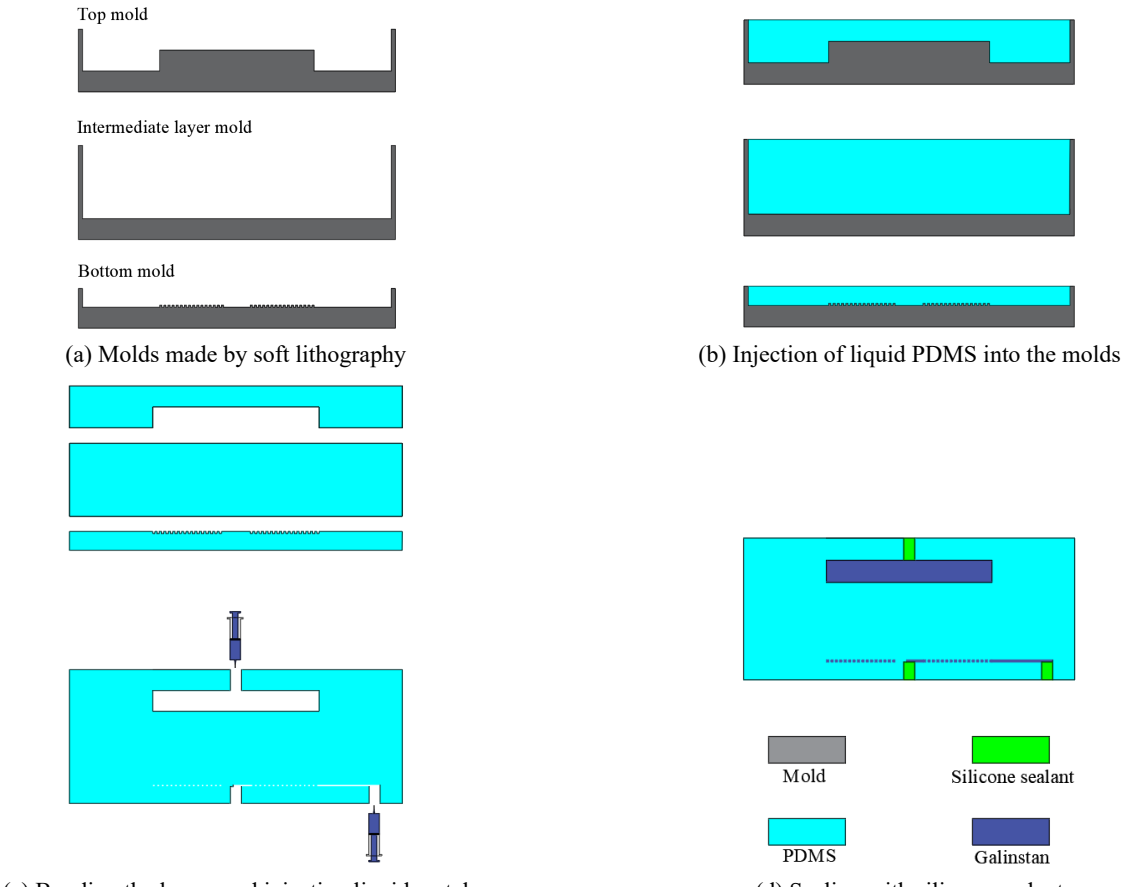

(a) Molds made by soft lithography

(b) Injection of liquid PDMS into the molds

(c) Bonding the layers and injecting liquid metal

(d) Sealing with silicone sealant

Fig. 8 The fabrication process of the sensor

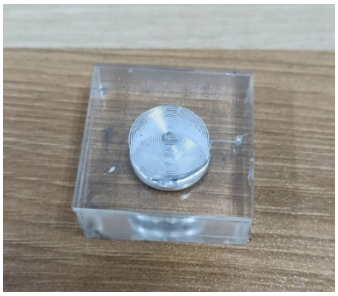

Fig. 9 Sensor sample filled with liquid metal

seconds, and are placed at 70°C for 15 minutes to make them permanently bonded (Ota 2018). On the molded PDMS microfluidic chip, a puncher is used to make two small holes with a diameter of 1mm at the inlet and outlet of the bottom spiral microfluidic channel and a small hole with a diameter of 1mm in the middle of the top layer for subsequent injection of liquid metal. As shown in Fig. 8(c), a syringe is used to inject liquid metal into the microfluidic channel in the bottom silicone rubber PDMS and the disc-shaped hole in the top layer.

Wires are used to connect with both ends of the bottom

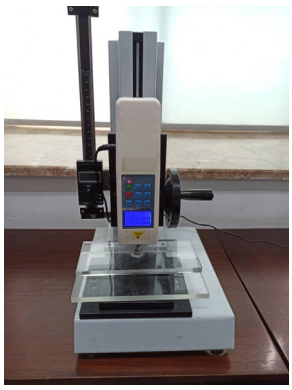

(a) Push-pull force gauge

(b) LCR digital bridge tester

Fig. 10 Experimental devices

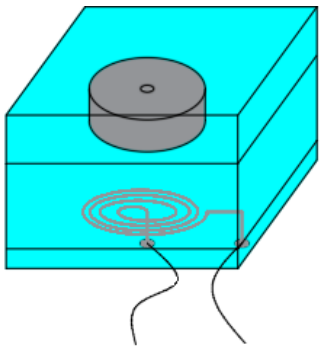

(a)

(b)

Fig. 11 (a) Schematic diagram of the first wiring method; (b) Physical diagram of the first wiring method

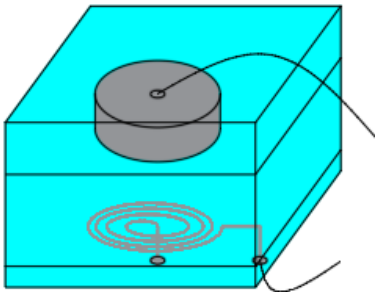

(a)

(b)

Fig. 12 (a) Schematic diagram of the second wiring method; (b) Physical diagram of the second wiring method

spiral micro channel, and the wire connections is sealed with Dow Corning 734 transparent flowable silicone sealant, as shown in Fig. 8(d). The sensor filled with liquid metal is shown in Fig. 9.

According to the previous work (Wang *et al*. 2018), the size of this sensor is designed. The dimension of the sensor s 30 mm × 30 mm × 12.8 mm with the intermediate layer thickness of 7 mm, the spiral microchannel length of about 527 mm, and the side length of the cross section of the microchannel is 0.2 mm.

4. Experiments and analysis

4.1 Experiments

To evaluate the response of the sensor, the experimental device shown in Fig. 10(a) is employed to measure the changes in resistance, capacitance and inductance under the applied normal pressure. The sensor developed in this paper is placed in a digital push-pull force gauge (HF1000, Sange (Chongqing) Instrument Co., Ltd.). The rated load of the digital push-pull force gauge can reach 1000 N with an accuracy of 0.01 N. A flat plastic pressure plate is installed on it. In addition, The LCR digital bridge tester (VC4092, Xi'an Shengli Instrument Co., Ltd.) is used to measure the sensor's resistance, capacitance and inductance under the applied normal pressure. The resistance measurement range of the LCR tester is 0.0001 Ω-1000 MΩ, the capacitance measurement range is 0.0001 pF-100 mF, the inductance measurement range is 0.0001 μH-10000 μH, and the basic accuracy is 0.05%.In order to study the change of resistance, capacitance and inductance of the sensor under the applied normal pressure, two different wiring methods are used. The first wiring method is shown in Fig. 11, which can be used to measure resistance and inductance. The second wiring method is shown in Fig. 12, which can be used to measure the capacitance of the sensor. In these two different wiring modes, the pressure plate of the sensor is slowly moved along the Z axis until the pressure reaches 100 kPa. In this process, the resistance, capacitance, and inductance values corresponding to different normal pressures are recorded.

4.2 Data analysis

It can be found from experimental data that the resistance of the sensor nonlinearly changes with the pressure, and the capacitance and inductance of the sensor approximately linearly change with the pressure. In this paper, the least square method is used to analyze the experimental data. The curve of sensor resistance vs pressure is shown in Fig. 13(a), the curve of capacitance of sensor against pressure is plotted in Fig. 13(b), and the curve of inductance against pressure is depicted in Fig. 13(c).

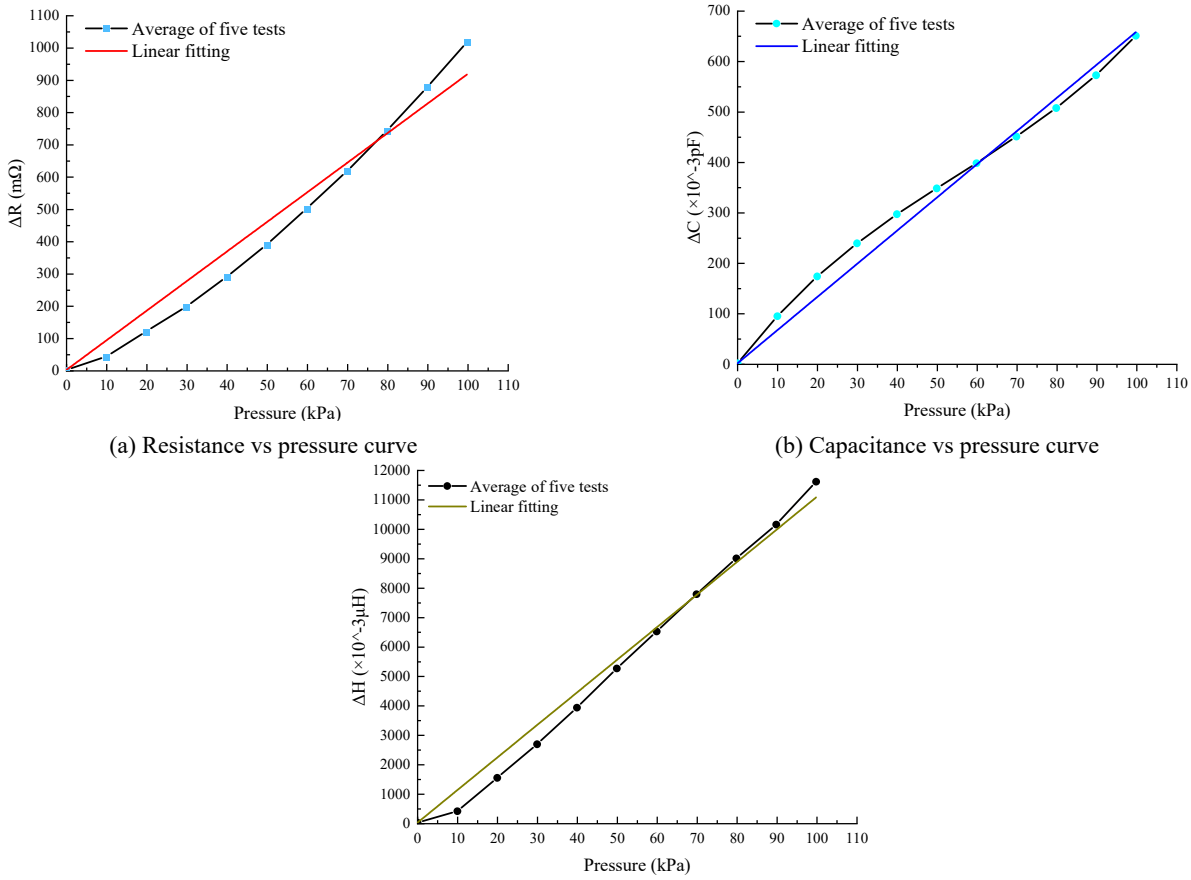

(a) Resistance vs pressure curve

(b) Capacitance vs pressure curve

(c) Inductance vs pressure curve

Fig. 13 Curves of resistance (a), capacitance (b) and inductance (c) vs pressure

Table 2 Fitting parameters of three pressure measurement indexes

	Resistance	Capacitance	Inductance
A	0	0	0
B	9.17299	6.58071	110.82471
R^2	0.98796	0.99805	0.99553

To compare with the linear fitting effect of three pressure measurement indexes, the linear fitting of resistance, capacitance, inductance and pressure is carried out by using the equation $y = A + Bx$. It can be seen from Table 2 that the correlation coefficient R^2 of resistance, capacitance and inductance is greater than 0.98, which indicates that the fitting effect of these three indicators is very good. Among them, the best fitting effect is the capacitance, and its correlation coefficient R^2 reaches 0.998, implying that the fitting curve can well reflect the change of the capacitance of the sensor vs the applied pressure.

In addition, the error bars of these three indicators of the pressure sensor in its pressure range are shown in Fig. 14. Obviously, the errors of the three measurement indicators in the pressure range of the sensor are very small.

5. Discussion

5.1 Cyclic load experiment of the sensor

Under the action of pressure, the cross section of the spiral microchannel of the sensor may deform, leading to change the resistance, capacitance and inductance of the sensor. The calibration experiment of pressure sensor is carried out by using the equipment shown in Fig. 10(a). The experimental data of this sensor under five loading and unloading cycles are shown in Fig. 15, and the partial enlarged diagram of the cyclic loading experimental data of three indexes (resistance, capacitance and inductance) is plotted in Fig. 15(f). It is easy to find from Fig. 15 that the experimental results of these three indexes little fluctuate.

5.2 Performance evaluation of three pressure measurement indexes

5.2.1 Hysteresis

The hysteresis of the chip reflects the degree of misalignment of the input and output curves in the positive stroke and the reverse stroke. Generally, the return error γ_H is used to evaluate the hysteresis phenomenon. The following formula is used to calculate the return error of three pressure measurement indicators (resistance, capacitance and inductance) during the five-cycle load experiments

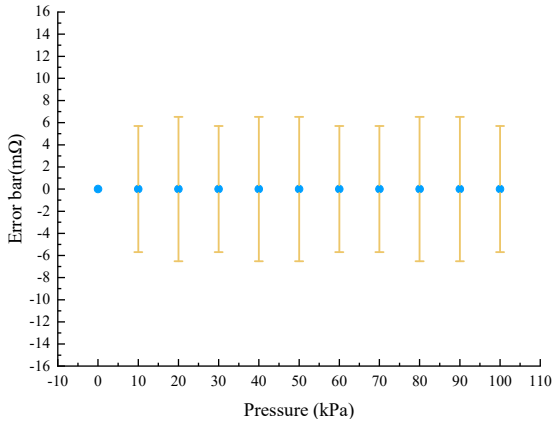

(a) Resistance error

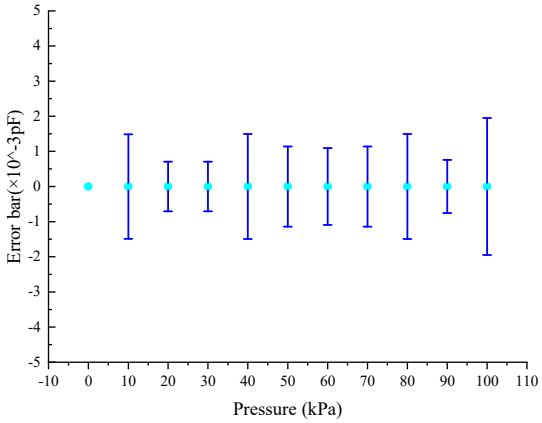

(b) Capacitance error

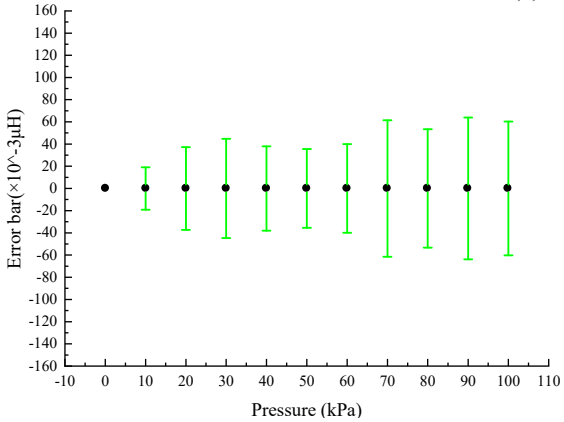

(c) Inductance error

Fig. 14 The error of the three indicators of the pressure sensor within its pressure range

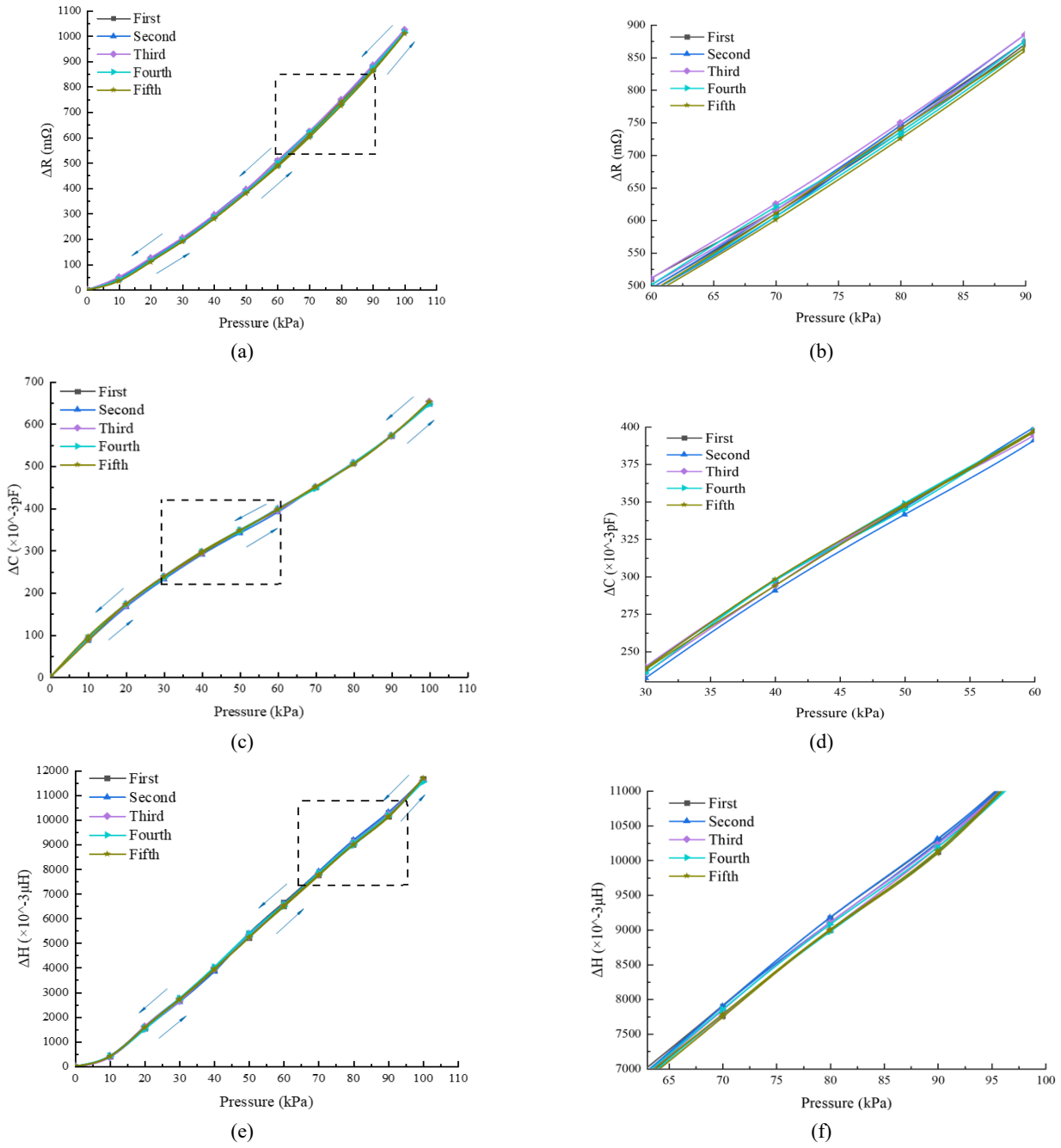

Fig. 15 The change of resistance (a), capacitance (c) and inductance (e) under cyclic load and their local enlarged diagram

$$\gamma_H = \left|\frac{\Delta_{H_{max}}}{y_{FS}}\right| \times 100\% \tag{33}$$

$$y_{FS} = |y_{max} - y_{min}| \tag{34}$$

where $\Delta_{H_{max}}$ is the maximum difference of the return curve; y_{FS} is the full-scale output value; y_{max} is the upper limit output value in the pressure measurement range; y_{min} is the lower limit output value in the pressure measurement range.

Table 3 shows the comparison of the return errors among these three pressure measurement indicators. It is found from Table 3 that the return errors γ_H of resistance, capacitance and inductance are all less than 1%. Therefore, it can be concluded that the three pressure measurement indicators of the sensor developed in this paper have good repeatability, and the accuracy of its measurement can still be guaranteed during long-term use. Among them, the return error of the capacitance is the smallest, indicating that the use of the capacitance for pressure sensing has the smallest hysteresis.

5.2.2 Repeatability

Repeatability γ_r reflects the random error of a sensor. This paper uses the following equation to evaluate the repeatability error of three pressure measurement indexes.

$$\gamma_r = \frac{3S}{y_{FS}} \times 100\% \tag{35}$$

Table 3 Analysis results of three pressure measurement indexes

	Resistance	Capacitance	Inductance
γ_H	0.98%	0.62%	0.81%
γ_r	0.65%	0.32%	0.41%
$\bar{S}_b$	0.76%	0.29%	0.79%
γ_L	8.89%	6.34%	4.32%

$$S = \sqrt{\frac{1}{2m}\left(\sum_{i=1}^{m} S_{li}^2 - \sum_{i=1}^{m} S_{Di}^2\right)} \tag{36}$$

$$S_{li} = \sqrt{\frac{1}{n-1}\sum_{j=1}^{n}\left(y_{lij} - \bar{y}_{li}\right)^2} \tag{37}$$

$$S_{Di} = \sqrt{\frac{1}{n-1}\sum_{j=1}^{n}\left(y_{Dij} - \bar{y}_{Di}\right)^2} \tag{38}$$

where S is the overall standard deviation of the sensor, S_{li} is the standard deviation of the positive stroke at each detection point, S_{Di} is the standard deviation of the reverse stroke at each detection point, m is the number of verification points in the entire pressure measurement range, n is the number of cyclic verifications.

Table 3 shows the comparison of the repeatability errors between these three pressure measurement indicators. It is found from Table 3 that the repeatability errors γ_f of resistance, capacitance and inductance are all less than 1%, implying there is basically no residual strain during the experiment. The best repeatability is capacitance, while the worst repeatability is resistance.

5.2.3 Periodic stability of sensitivity

The ratio of the absolute value of sensitivity difference between two adjacent periods to the sensitivity of this verification is called sensitivity periodic stability, which can be calculated by

$$S_b = \left|\frac{b - b_0}{b}\right| \times 100\% \tag{39}$$

where S_b is the periodic stability of sensitivity, b is the sensitivity of the sensor, and b_0 is the sensitivity of the sensor in the last cycle.

Then, the average stability of the sensor sensitivity in five cycles is as follows

$$\bar{S}_b = (S_{b1} + S_{b2} + S_{b3} + S_{b4})/4 \tag{40}$$

where $S_{bi}\ (i = 1, 2, 3, 4)$ is the periodic stability of sensitivity during five times of periodic loading.

Obviously, it can be seen from Table 3 that the sensitivity periodic stability of capacitor is the best, $\bar{S}_b$ is only 0.29%, and the sensitivity periodic stability of inductor is the worst.

5.2.4 Linearity

Linearity is an index used to evaluate the deviation degree of experimental data and sensor characteristic curve. It is usually expressed by the ratio of the maximum deviation Δ_{lmax} between the actual data and the fitting curve to the full-scale output y_{Fs}. It can be written as

$$\gamma_L = \left|\frac{\Delta_{lmax}}{y_{FS}}\right| \times 100\% \tag{41}$$

where Δ_{lmax} is the maximum deviation between the arithmetic mean value of the output value and the selected working line, and y_{FS} is the difference between the upper and lower pressure values of the measurement range.

As can be seen from Table 3, the inductance has the best linearity, followed by capacitance and resistance in turns.

5.3 Comparison between experimental data and theoretical values

It can be seen from Fig. 16(a) that when the pressure is in the range of 0-50 kPa, the theoretical value of the resistance change is in good agreement with the experimental data, while in the range of 50-100 kPa, the theoretical value is slightly lower than the experimental data, and the difference between the theoretical value and the experimental data tends to increase as the pressure increases. Although there are differences between the theoretical value and the experimental value of the resistance, the trend of theoretical values is consistent with the experimental results. It is found from Fig. 16(a) that the slopes of the theoretical curve and the experimental curve gradually increase as the pressure increases. The reason is that as the pressure increases, the microchannel gradually approaches collapse, and the cross-sectional change increases significantly.

When the pressure is between 0-30 kPa, the theoretical value of the capacitance change is in good agreement with the experimental value, as shown in Fig. 16(b). When the pressure exceeds 30 kPa, the theoretical value and the experimental value are slightly different. Obviously, the difference between the theoretical value and the experimental value gradually increases as the applied pressure increases, but the trend of the theoretical values and the experimental values is still basically consistent.

In addition, we studied the relative error between theoretical and experimental results. Both the resistance and the capacitance have the maximum relative error when the pressure is 10 kPa, and the absolute value of the relative error at other points is less than 20%, as shown in Fig. 17. This implies that the developed theoretical models of resistance and capacitance can be used to explain the performance of the sensor, although it cannot explain all the observation data well.

Although the principle of inductance change is investigated in Section 2.3, the expression of $k(x)$ in Eq. (22) is difficult to obtain and is very complicated, depending on the geometry of the coil and the target

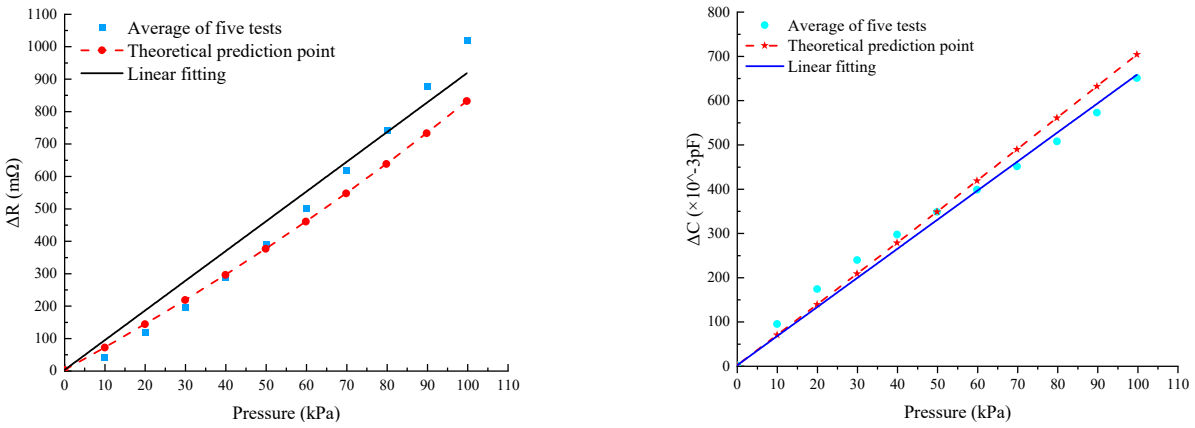

(a) Comparison of experimental and theoretical values of resistance (b) Comparison of experimental and theoretical values of capacitance

Fig. 16 Comparison of theoretical and experimental values

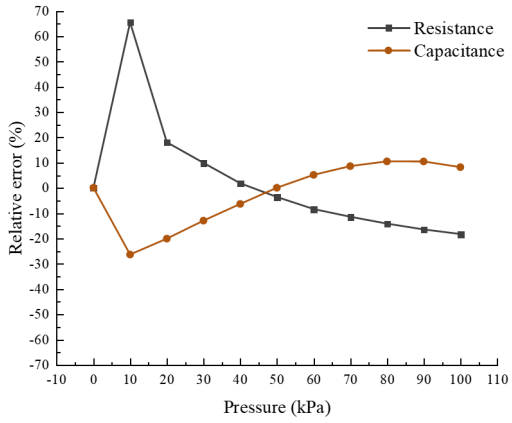

Fig. 17 Relative error between theoretical and experimental results

properties. Therefore, the theoretical value of the inductance change is difficult to obtain, and the comparison of the theoretical value and the experimental of value inductance change is not investigated in this paper.

6. Conclusions

The pressure sensor developed in this paper is mainly composed of a polydimethylsiloxane (PDMS) elastomer, a cylindrical cavity filled with liquid metal on the top and a spiral microchannel filled with liquid metal on the bottom. This is a new type of flexible pressure sensor structure. The resistance, capacitance and inductance changes of this sensor under pressure can be measured through two different wiring methods.

Five cyclic loading experiments were carried out on the pressure sensor, and the hysteresis, repeatability, sensitivity cycle stability and linearity of these three pressure measurement indexes were compared and analyzed. It is found that the repeatability error and return error of these three pressure measurement indexes are less than 1%, so it can be concluded that there is basically no residual strain when the sensor is unloaded and reloaded during the experiment. Among them, the repeatability of the capacitance is the best and the hysteresis is the smallest. However, the linearity of the capacitance is the worst, while the linearity of the inductor is the best. In addition, in order to calibrate the sensor, the average value of the three pressure measurement indexes in the five cyclic load tests was linearly fitted. The results show that the fitting effect of the capacitance is the best, while the fitting effect of the resistance is the worst.

Based on linear elastic fracture mechanics, the cross-sectional changes of the sensor microchannel under pressure are theoretically analyzed, and the changes of resistance and capacitance with pressure are deduced and verified with experimental data. In the range of 0-50kPa, the theoretical values of resistance are in good agreement with the experimental data of resistance, while in the range of 50-100 kPa, the theoretical values are slightly different from the experimental data, and the difference between the theoretical values and experimental data increases with increasing the applied pressure. Similarly, the theoretical values of the capacitance are close to the experimental data in the range of 0-30 kPa, and the difference between the theoretical value and experimental data increases with increasing the applied pressure when the pressure exceeds 30 kPa.

In this paper, the spiral microchannel filled with liquid metal is used to replace the rigid metal coil in the traditional flexible eddy current sensor to improve the flexibility and mechanical durability of the sensor. The experimental results show that the inductance linearly changes with an increase in pressure in the range of 0-100 kPa, and it has good repeatability, linearity and low hysteresis.

In the future work, we will further analyze the principle of sensor inductance change and will establish a more accurate model to guide the design of the sensor.

Acknowledgments

The work is supported by the National Natural Science Foundation of China (Nos. 52027814, 51839009).

References

Ali, M.M., Narakathu, B.B., Emamian, S., Chlaihawi, A.A., Aljanabi, F., Maddipatla, D., Bazuin, B.J. and Atashbar, M.Z. (2016), "Eutectic Ga-In liquid metal based flexible capacitive pressure sensor", *Proceedings of IEEE Sensors Conference*, Orlando, FL, USA, October. https://doi.org/10.1109/ICSENS.2016.7808515

Chuang, C.H., Liou, Y.R. and Shieh, M.Y. (2012), "Flexible tactile sensor array for foot pressure mapping system in a biped robot", *Smart Struct. Syst., Int. J.*, **9**(6), 535-547. https://doi.org/10.12989/sss.2012.9.6.535

Gao, M. and Gui, L. (2014), "A liquid metal based capacitive microsensor", *Proceedings of ASME 12th International Conference*, Chicago, IL, USA, August. https://doi.org/10.1115/ICNMM2014-21205

Gao, Y.J., Ota, H., Schaler, E.W., Chen, K., Zhao, A., Gao, W., Fahad, H.M., Leng, Y., Zheng, A., Xiong, F., Zhang, C., Tai, L., Zhao, P., Fearing, R.S. and Javey, A. (2017), "Wearable microfluidic diaphragm pressure sensor for health and tactile touch monitoring", *Adv. Mater.*, **29**(39), 1701985. https://doi.org/10.1002/adma.201701985

Hu, H., Shaikh, K. and Liu, C. (2007), "Super flexible sensor skin using liquid metal as interconnect", *Proceedings of IEEE Sensors Conference*, Atlanta, GA, USA, October. https://doi.org/10.1109/ICSENS.2007.4388525

Huang, Y., Fang, D., Wu, C., Wang, W.H., Guo, X.H. and Liu, P. (2016), "A flexible touch-pressure sensor array with wireless transmission system for robotic skin", *Rev. Sci. Instrum.*, **87**(6), 065007. https://doi.org/10.1063/1.4954199

Jung, T. and Yang, S. (2015), "Highly stable liquid metal-based pressure sensor integrated with a microfluidic channel", *Sensors*, **15**(5), 11823-11835. https://doi.org/10.3390/s150511823

Kawasetsu, T., Horii, T., Ishihara, H. and Asada, M. (2017), "Size dependency in sensor response of a flexible tactile sensor based on inductance measurement", *Proceedings of IEEE Sensors Conference*, Glasgow, UK, October. https://doi.org/10.1109/ICSENS.2017.8233908

Kawasetsu, T., Horii, T., Ishihara, H. and Asada, M. (2018), "Flexible tri-axis tactile sensor using spiral inductor and magnetorheological elastomer", *IEEE Sensors J.*, **18**(14), 5834-5841. https://doi.org/10.1109/JSEN.2018.2844194

Li, K., Turcotte, K. and Veres, T. (2019), "Stretchable strain sensors based on thermoplastic elastomer microfluidics embedded with liquid metal", *Proceedings of IEEE Sensors Conference*, Montreal, Canada, October. https://doi.org/10.1109/SENSORS43011.2019.8956780

Ota, H. (2018), "Liquid-state environment sensors using liquid metal", *ECS Trans.*, **86**(16), 31-38. https://doi.org/10.1149/08616.0031ecst

Palmer, M.C., O'Rourke, T.D., Olson, N.A., Abdoun, T., Ha, D. and O'Rourke, M.J. (2009), "Tactile pressure sensors for soil-structure interaction assessment", *J. Geotech. Geoenviron. Eng.*, **135**(11), 1638-1645. https://doi.org/10.1061/(ASCE)GT.1943-5606.0000143

Park, Y.L., Majidi, C., Kramer, R., Brard, P. and Wood, R.J. (2010), "Hyperelastic pressure sensing with a liquid-embedded elastomer", *J. Micromech. Microeng.*, **20**(12), 125029. https://doi.org/10.1088/0960-1317/20/12/125029

Qiao, Z.Y. (2021), "Calculation and Simulation of planar spiral inductor based on flexible substrate", *Shipboard Electron. Countermeas.*, **44**(1), 116-120. https://doi.org/10.16426/j.cnki.jcdzdk.2021.01.024

Rudgers, A.J. (1988), "Equivalent-network representations of the generalized Hooke's law for isotropic materials", *J. Acoust. Soc. Am.*, **83**(2), 483-486. https://doi.org/10.1121/1.396142

Ryu, D., Loh, K.J., Ireland, R., Karimzada, M., Yaghmaie, F. and Gusman, A.M. (2011), "In situ reduction of gold nanoparticles in PDMS matrices and applications for large strain sensing", *Smart Struct. Syst., Int. J.*, **8**(5), 471-486. https://doi.org/10.12989/sss.2011.8.5.471

Shi, X. and Cheng, C.H. (2013), "Artificial hair cell sensors using liquid metal alloy as piezoresistors", *Proceedings of the 8th Annual IEEE International Conference on Nano/Micro Engineered and Molecular Systems*, Suzhou, China, April. https://doi.org/10.1109/NEMS.2013.6559886

Shou, Y.D., Zhou, X.P., Chang, Q.P. and Liu, C. (2021), "An innovative liquid metal-based pressure sensor with its application in geotechnical engineering", *Smart Struct. Syst., Int. J.*, **27**(1), 89-99. https://doi.org/10.12989/sss.2021.27.1.089

Shull, K.R. (2002), "Contact mechanics and the adhesion of soft solids", *Mater. Sci. Eng. R.*, **36**(1), 1-45. https://doi.org/10.1016/S0927-796X(01)00039-0

Springman, S.M., Nater, P., Chikatamarla, R. and Laue, J. (2002), "Use of flexible tactile pressure sensors in geotechnical centrifuges", *Proceedings of International Conference Physical Modelling Geotechnics*, Netherlands, January. http://pascal-francis.inist.fr/vibad/index.php?action=getRecordDetail&idt=15076914

Tada, H., Paris, P.C. and Irwin, G.R. (2000), *The Stress Analysis of Cracks Handbook*, Third Edition, ASME Press, New York, NY, USA.

Wang, H.B., Lin, Y.B., Li, W. and Feng, Z.H. (2014), "Design of ultrastable and high resolution eddy-current displacement sensor system", *Proceedings of the 40th Annual Conference of the IEEE Industrial Electronics Society*, Dallas, TX, USA, October. https://doi.org/10.1109/IECON.2014.7048828

Wang, H.B., Kow, J.W., Boer, G.D., Jones, D., Alazmani, A. and Culmer, P. (2017), "A low-cost, high-performance, soft tri-axis tactile sensor based on eddy-current effect", *Proceedings of IEEE Sensors Conference*, Glasgow, UK, October. https://doi.org/10.1109/ICSENS.2017.8234098

Wang, H.B., Kow, J.W., Raske, N., de Boer, G, Ghajari, M., Hewson, R. and Alazmani, A. (2018), "Robust and high-performance soft inductive tactile sensors based on the Eddy-current effect", *Sens. Actuat. A: Phys.*, **271**, 44-52. https://doi.org/10.1016/j.sna.2017.12.060

Won, D.J., Baek, S., Kim, H. and Kim, J. (2015), "Arrayed-type touch sensor using micro liquid metal droplets with large dynamic range and high sensitivity", *Sens. Actuat. A: Phys.*, **235**, 151-157. https://doi.org/10.1016/j.sna.2015.09.044

Wong, R.D.P., Posner, J.D. and Santos, V.J. (2012), "Flexible microfluidic normal force sensor skin for tactile feedback", *Sens. Actuat. A: Phys.*, **179**, 62-69. https://doi.org/10.1016/j.sna.2012.03.023

Wu, J.C., Hu, X.L., Sun, M.J. and Hua, S. (2012), "Research Status and Prospect of Strain Monitoring Method of Geotechnical Engineering", *Adv. Mater. Res.*, **594-597**, 532-541. https://doi.org/10.4028/www.scientific.net/AMR.594-597.532

Xu, X.M., Soga, K., Nawaz, S., Moss, N., Bowers, K. and Gajia, M. (2015), "Performance monitoring of timber structures in underground construction using wireless SmartPlank", *Smart Struct. Syst., Int. J.*, **15**(3), 769-785. https://doi.org/10.12989/sss.2015.15.3.769

Yang, X.F., Wang, Y.S. and Qing, X.L. (2018), "A flexible capacitive pressure sensor based on ionic liquid", *Sensors*, **18**(7), 2395. https://doi.org/10.3390/s18072395

Zeng, J. (2018), "Pressure sensor antenna based on liquid metal material and RF technology", Mater Dissertation; Chongqing University, Chongqing, China.

Zhang, L.J., Gao, M., Wang, R.H., Deng, Z.S. and Gui, L. (2019), "Stretchable pressure sensor with leakage-free liquid-metal

electrodes", *Sensors*, **19**(6), 1316.
https://doi.org/10.3390/s19061316
Zhi, Z., Wang, H.Z. and Ou, J.P. (2006), "A new kind of FBG-based soil-pressure sensor", *Proceedings of Optical Fiber Sensors Conference*, Cancun, Mexico, October.
https://doi.org/10.1364/OFS.2006.ThE90
Zhou, X.P., Deng, R.S. and Zhu, J.Y. (2018), "Three-layer-stacked pressure sensor with a liquid metal-embedded elastomer", *J. Micromech. Microeng.*, **28**(8), 085020.
https://doi.org/10.1088/1361-6439/aac13c
Zhou, X.P., Liu, C. and Zhao, K. (2020), "A novel liquid metal sensor with three microchannels embedded in elastomer", *Smart Mater. Struct.*, **29**(4), 1-18.
https://doi.org/10.1088/1361-665X/ab7433

HJ